

Two-Dimensional Semiconductors for Photodetection

Jian Sun¹, Cheng Yang², Fei Yao³, and Huamin Li⁴

¹School of Physics and Electronics, Central South University, Changsha, China

²School of Physics and Electronics, Shandong Normal University, Jinan, China

³Department of Materials Design and Innovation, University at Buffalo, The State University of New York, Buffalo, NY, USA

⁴Department of Electrical Engineering, University at Buffalo, The State University of New York, Buffalo, NY, USA

Abstract

Since the discovery of graphene, two-dimensional (2D) semiconductors have attracted intensive interest due to their unique properties. In particular, 2D semiconductors possess unique physics and superior performance for light–matter interactions in a comparison with three-dimensional (3D) bulk counterparts. In this article, the general electronic and optoelectronic properties of 2D semiconductors will be firstly introduced. Then the technical approaches for tuning their electronic properties including both energy bandgap engineering and doping will be presented. Electrical contacts of 2D semiconductor devices as another technical challenge will also be discussed. Finally, the application of 2D semiconductors in photodetectors, including both the light–matter interaction mechanisms and the metric benchmarking of recent advances will be summarized.

Keywords 2D semiconductors; photodetection; band gap engineering; doping; contact engineering

1	Introduction	1
2	2H-Phase TMDC Semiconductors	3
3	Bandgap Engineering	4
4	Doping	6
5	Contact Engineering	10
6	Photodetectors	12
7	Summary and Perspective	17
	Acknowledgments	18
	Related Articles	18
	References	19

1 Introduction

With the rise of graphene (Gr) from 2004 [1], two-dimensional (2D) materials have drawn great attention for broad disciplines. In addition to graphene, other representative

2D materials include transition metal dichalcogenides (TMDCs), group III or IV chalcogenides (GaSe, GeSe, etc.), and transition-metal carbides, nitrides, and carbonitrides (MXenes) [2–4]. Especially

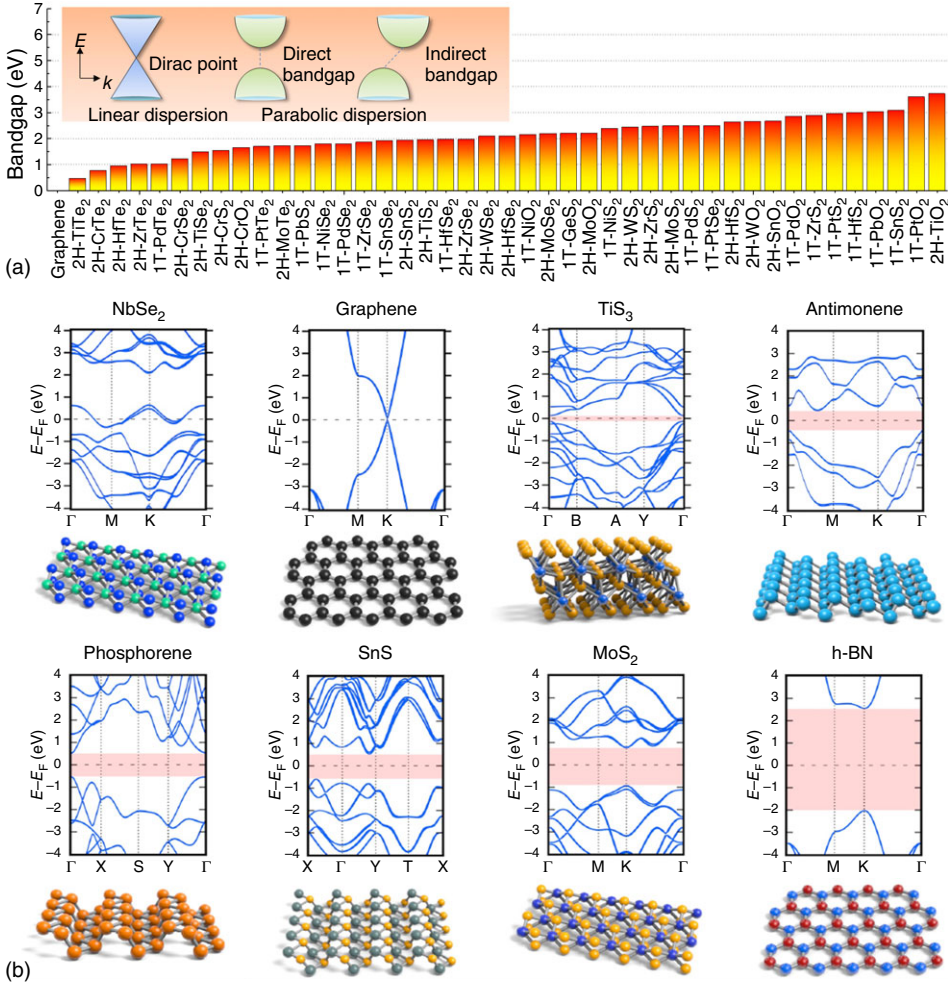


Figure 1 (a) Schematic and summary of the bandgaps of different 2D materials. Inset: A comparison of linear dispersion and parabolic dispersion (including both direct and indirect bandgap semiconductors) in energy band diagrams. Source: Data adapted from Refs. [5, 6]. (b) Band diagrams and lattice structure of selected 2D materials ordered by bandgap from narrow to large. Source: Reproduced with permission from Ref. [5] Copyright 2017, Royal Society of Chemistry.

for nanoelectronic and optoelectronic perspectives, the rich material chemistry and different structural phases grant 2D materials a variety of electronic band structures covering from metals (e.g. Gr) to semiconductors (e.g. phosphorene and MoS₂) and insulators (e.g. h-BN) [5, 6], as shown in Figure 1. High-quality monolayer and few-layer 2D flakes can be mechanically isolated from their bulk crystals using scotch-tape-based exfoliation methods, which are widely used in fundamental

physics investigations and device prototypes demonstration. However, this method is time consuming and not suitable for large-scale preparation for electronics and optoelectronics. Therefore, vapor-phase deposition methods such as chemical vapor deposition (CVD), metal-organic chemical vapor deposition (MOCVD), and physical vapor deposition, have been developed as the more promising approaches to produce monolayer or few-layer 2D materials with good quality, low cost, and scale-up

capability [7]. Compared to the conventional three-dimensional (3D) bulk materials, the band structure of layered 2D materials can be directly affected by the unique interlayer van der Waals (vdW) interaction, which is generally composed of three different intermolecular interactions: dipole–dipole interaction (Keesom force), dipole–induced dipole interaction (Debye force), and instantaneous dipole–induced dipole interaction (London force). The typical value of the vdW interaction strength is about $0.1\text{--}10\text{ kJ mol}^{-1}$ which is much smaller than that of the ionic or covalent bonds. Accordingly, the vdW gap, also known as the 2D layer-to-layer distance or interlayer spacing, is relatively larger compared to the ionic or covalent bond length [8].

Among the abundant 2D materials, 2D semiconductors stand out as a promising material candidate for various applications, including high-end electronics, spintronics, optoelectronics, energy harvesting, flexible electronics, DNA sequencing, and personalized medicine [9–11]. Especially for light–matter interactions, 2D semiconductors possess unique physics and superior performance in a comparison with 3D bulk counterparts. In this article, we specifically emphasize on the 2D semiconducting TMDCs, known as one of the most representative 2D semiconductors, and provide a brief review from the perspective of their electronic engineering and photodetector application. In the following sections, we will first summarize the general electronic and optoelectronic properties of 2D TMDC semiconductors, then discuss the approaches for their electronic band structure engineering including both the energy bandgap tuning and carrier polarity and concentration tuning (i.e. doping). Next, we will address the fundamental challenges in metal–semiconductor contacts which limit the material potential and device performance of 2D TMDC semiconductors. Finally, we will discuss the application of 2D TMDC semiconductors in photodetectors, including both

the light–matter interaction mechanisms and the metric benchmarking of recent advances.

2 2H-Phase TMDC Semiconductors

The individual layers of TMDC materials consist of three atomic planes (chalcogen–metal–chalcogen). As such, TMDCs are often expressed with a chemical composition of MX_2 where M and X represent transition metals (e.g. Mo, W, Hf, and Zr) and chalcogen elements (e.g. S, Se, and Te), respectively. The coordination of the transition metal atoms can be trigonal prismatic (2H) or octahedral (1T), corresponding to two distinctive structural phases, i.e. a 2H phase with an ABA stacking order and a 1T phases with an ABC stacking order [12]. In general, TMDCs involving group VI transition metals (Mo or W) combined with S and Se (i.e. MoS_2 , MoSe_2 , WS_2 , and WSe_2) exhibit semiconducting properties in their thermodynamically stable 2H phases. On the other hand, their 1T phase is generally metallic to semimetallic.

Due to the semiconducting nature, the thermodynamically stable 2H phase of 2D TMDCs such as MoS_2 , MoSe_2 , WS_2 , and WSe_2 have been widely applied in electronic devices. Compared to the conventional bulky semiconductors which charge carrier mobility degrades significantly as the physical thickness reduces to a few nanometers, 2D semiconductors have the natural advantages to maintain excellent carrier transport even for atomically thin layers at sub-1-nm scale. Taking MoS_2 as an example, its high electron mobility within a monolayer form has been exploited to build miniaturized transistors, which can reduce direct source–drain tunneling current and minimize the conventional short-channel effect [13]. The upper limit of the performance of a MoS_2 field-effect transistor (FET) has been evaluated in theory [14, 15], and the MoS_2 FETs with 10-nm gate length has been successfully

demonstrated with good subthreshold swing (~ 80 mV/decade, close to the fundamental limit of 60 mV/decade at room temperature) and high on-state current density (over $400 \mu\text{A } \mu\text{m}^{-1}$) [13, 16]. Very recently, the ultimately scaled MoS_2 FETs with a 1-nm or even sub-1-nm gate length have been achieved experimentally using innovative architecture design, including a nanotube as the gate [17] or the transferred vdW electrodes in a vertical-stacking structure [18].

2D TMDCs are also a good material candidate for optoelectronic applications due to their strong response to light illumination [4, 11]. For example, a monolayer TMDC with the sub-nanometer (6.5 \AA) thickness can have $\sim 10\%$ photon absorbance in visible spectrum which is equivalent to a 50-nm-thick Si layer or a 15-nm-thick GaAs layer, generate electrical currents as high as 4.5 mA cm^{-2} , and provide ultra-high power densities of up to 2.5 MW kg^{-1} or 10 MW l^{-1} which is far superior compared to record thin-film solar cells based on Si (2.5 kW kg^{-1} or 5.9 kW l^{-1}) or GaAs (54 kW kg^{-1} or 290 kW l^{-1}) [19]. By integrating with a silicon substrate to form a 2D/3D type-II heterojunction, the light-to-electricity power conversion efficiency of a monolayer MoS_2 can be improved to 5.23% [20].

3 Bandgap Engineering

Energy bandgap, defined as the energy difference between the conduction band minima (CBM) and the valence band maxima (VBM), is one of the most important parameters to govern the physical properties of 2D semiconductors and the relevant performance in their electronic and optoelectronic applications. For example, the energy bandgap directly determines the minimum phonon energy (or the maximum wavelength) of the light source that the material can absorb. The direct bandgap semiconductors are preferred in general for optoelectronic applications due to their high efficiency of light-to-electricity conversion compared to

the indirect bandgap semiconductors. Here, we briefly summarize the major technologies to engineer the bandgap of 2D TMDC materials, including layer number, strain, dielectric environment, pressure, external electric field, atom substitution, and phase change, as shown in Figure 2.

3.1 Layer Number or Thickness

Here we take 2D semiconducting TMDCs as examples, including 2H MoS_2 , MoSe_2 , WS_2 , and WSe_2 . As the layer number (or thickness) decreases from 4 layers to monolayer, the conduction and valence band edges evolve as well, and the indirect bandgap changes to the direct bandgap in the monolayer form (see an example of MoS_2 in Figure 2a). When the layer number is over 3 or 4 layers, the energy band structure is in general consistent with the case of the bulk counterparts [21, 27]. Such strong dependence of the 2D electronic band structures on the layer number or thickness is attributed to the interlayer coupling and quantum confinement [28].

3.2 Strain

Because the natural advantages of 2D TMDCs in flexibility and stretchability, strain effect, or mechanical deformation, are exploited as an effective approach to tune the band structure of 2D TMDCs. In general, three types of strain can be applied for 2D semiconductors [29]: (i) homogeneous uniaxial strain induced by bending, rolling, or elongation; (ii) homogeneous biaxial strain induced by thermal expansion and piezoelectric straining; and (iii) inhomogeneous local strain induced by laser illumination, wrinkling, and nanostructure support. Taking monolayer MoS_2 as an example, a decrease in the bandgap is obtained with increasing tensile strain [30], which can further develop to a semiconductor-to-metal phase transition (see Figure 2b) [31]. Other consequences, such as the shift of CBM and VBM and a direct-to-indirect bandgap transition have also been reported [22, 30, 32].

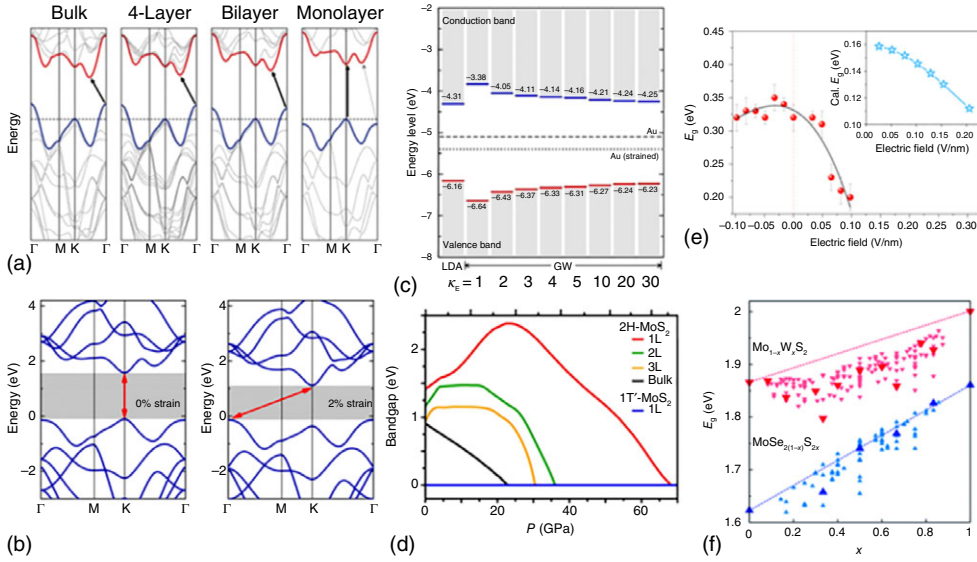


Figure 2 Approaches for modulating the bandgap of TMDC materials: (a) layer number (for MoS_2). Source: Reproduced with permission from Ref. [21] Copyright 2010, American Chemical Society. (b) Strain effect (for MoS_2). Source: Reproduced from Ref. [22]/Springer Nature/CC BY 4.0. (c) Dielectric environment (for MoS_2). Source: Reproduced from Ref. [23]/Springer Nature/CC BY 4.0. (d) Pressure (for MoS_2). Source: Reproduced with permission from Ref. [24] Copyright 2014, American Chemical Society. (e) External electric field (for black phosphorus). Source: Reproduced with permission from Ref. [25] Copyright 2017, American Chemical Society. (f) Concentration ratio for alloys. Source: Reproduced with permission from Ref. [26] Copyright 2014, Royal Society of Chemistry.

3.3 Dielectric Environment

It is known that the bandgap of a semiconductor is an intrinsic property independent of the environments. However, it is found that, due to an environmental dielectric screening (EDS) effect on the quasiparticle renormalization, a bandgap reduction can occur in 2D TMDCs. For instance, it is theoretically reported that the bandgap of monolayer MoS_2 in a both-side dielectric system can rapidly reduce when an effective environmental dielectric constant ranges up to 5 (see Figure 2c). In other words, the presence of a dielectric material with a moderate dielectric constant is capable of effectively modulating the monolayer MoS_2 bandgap [23].

3.4 Pressure

With an increase in pressure, a structural lattice distortion and an electronic transition

from the semiconducting state to metallic state can occur in a multilayer MoS_2 . As the interlayer spacing reduces, the electronic charge moves away from the S atoms and accumulates on the Mo atoms, suggesting a charge redistribution and thus an enhanced interlayer S–S interaction, compared to the weak vdW interaction at zero-pressure condition. Meanwhile, the degeneracy in the bands of the unstrained structure is lifted with the enhanced interlayer interaction under the pressure. Both CBM and VBM move toward the Fermi level, leading to a reduction of the bandgap and eventually the semiconducting-to-metallic state transition with zero bandgap (see Figure 2d) [24, 33]. On the other hand, for the monolayer MoS_2 , a direct-to-indirect bandgap transition under hydrostatic pressure at room temperature has been demonstrated in both theories and experiments, which was attributed to a K– Λ crossover in the conduction band [34].

Because of the absence of interlayer coupling in the monolayer structure, this transition mechanism is considered as an intrinsic intralayer nature only within the monolayers.

3.5 External Electric Field

An external electric field applied through a capacitor structure, also known as electrostatic gating, is a convenient way to provide a continuous tuning of a variety of electronic properties, including the energy band gap. For instance, the reduced bandgap from 0.31 to 0.20 eV has been measured in the few-layer black phosphorus (BP) subjected to the application of electrical field (see Figure 2e) [25], which is attributed to the shift of working spectral range by giant Stark effect and the multiphoton adsorptions by sub-band transition. For a monolayer ReSe₂ on a back-gated Gr, both the electronic and optical bandgap (E_g and E_{opt}), as well as the exciton binding energies (E_b), can be tuned by varying the applied gate voltage, which is mainly attributed to a screening effect from gate-controlled free carriers in Gr [35].

3.6 Alloying Effect

In addition to tuning the band structure by adjusting the external environment, a more straightforward method is to change the conditions of 2D semiconductors themselves, e.g. by alloying with other 2D semiconductors [36]. Most of the reported alloying has been realized using CVD method by mixing and substituting alloying components in stoichiometric ratio. Taking MoTe₂ as an example, an alloy of V_{1-x}Mo_xTe₂ can be formed by substituting Mo with V as a foreign element [26]. As the concentration of V increases, the Fermi level moves deeper into the valence band. This shift can lead to a heavy doping of V_{1-x}Mo_xTe₂, and consequently, a Mott semiconductor-metal transition. Other examples include Mo_{1-x}W_xS₂ and MoSe_{2(1-x)}S_{2x} alloys where Mo and Se are the foreign elements, respectively (see Figure 2f)

[26]. It is worth mentioning that the alloying in both metal and chalcogenide sites causes the comprehensive tuning of the electronic structures of TMDCs, leading to the doping effect at the same time, which will be discussed in the next section. Sometimes, the tuning of band gap requires a higher substitution concentration. For instance, the bandgap of Mo_{1-x}W_xSe₂ remains unchanged until a high W content up to 25% [37].

3.7 Phase transition

2D semiconductors possess different crystalline phases based on the arrangement of atoms. Two common structural phases include the 2H semiconducting phase with an ABA stacking order and the 1T metallic phase with an ABC stacking order. Depending on the particular combination of the elements, the thermodynamically stable phase can be either the 2H or 1T phase. It is shown in Figure 1 that the bandgap of 2D materials can be changed by switching the phases between 2H and 1T. In general, these phase changes are introduced by external modulations, such as surface doping, electrostatic doping, plasma treatment, and pressure [38].

4 Doping

Theoretically, intrinsic semiconductors are not conductive. At room temperature, electrons get enough energy to be excited across the forbidden gap into the conduction band. The numbers of electron and hole are equal and at relatively low density. Doping is a primary technique to precisely control electrical properties for semiconductors. For conventional thin films, substitutions of a small number of atoms with foreign atoms can change both dominant carrier type and concentration. This process is extremely effective. Substituting 1 ppm atoms with phosphorus/boron in intrinsic silicon modulates the dominant carrier to electron/hole and enhances the electron/hole density by

one million times. To define device structure and circuit elements, doping is normally required after the growth of thin film in selected areas. The techniques involved are diffusion and ion implantation. However, they are not compatible with 2D semiconductors, as 2D lattice cannot survive at the high temperature of diffusion or under the bombardments of high-energy ions. Hence, alternative doping techniques are urgently desired for 2D semiconductors.

4.1 Substitutional Doping

Alternatively, substitution during the growth of 2D semiconductors has been commonly utilized to dope 2D semiconductors by direct addition of dopants in the raw materials. For instance, the non-metallic atoms such as As, Se, and Te with low melting points are added to dope BP, which switches the dominant carrier type of BP from pristine p-type into n-type [39]. As aforementioned, substitutional doping, i.e. alloying, is able to tune the band gap of BP with the increased doping density. Band gap of BP is nearly reduced by two times to 0.15 eV by As-doping of 0.83% atomic ratio. Substitutional doping is widely applied to tune the electronic properties of TMDCs. The foreign atoms can substitute the atoms at either transition metal sites or chalcogen sites as plotted in Figure 3a, which act as donors and acceptors depending on their relative valency.

4.1.1 Transition Metal Substitution

4.1.1.1 p-Doping In TMDCs, transition metal atoms can be replaced by foreign atoms. These atoms with comparable radii to transition metals are chosen in order to avoid considerable distortion to 2D lattice structure. Generally, these substitutional atoms with less valence electrons than transition metals (Mo, W) lead to the p-type doping. The effects and the doping polarity of the substitutional dopant atoms can be clearly revealed using first-principle simulations. Experimentally, p-type doping has

been facilitated with Nb and V by CVD with NbCl_5 [40] or Nb_2O_5 [41] as Nb source, by chemical vapor transport (CVT) with Nb metal [42], and by CVD with $\text{NH}_4\text{H}_2\text{W}_{12}\text{O}_{40}$ and NH_4VO_3 as V precursors [43]. Positive shift of the threshold voltage is obtained in the transistor devices made of p-doped TMDCs. Pronounced red shifts and peak broadening in photoluminescence (PL) peaks have been identified in Nb-doped TMDCs, such as MoS_2 , WS_2 , and WSe_2 [40]. Heavy Nb-doping of 19% was reported in monolayer MoS_2 grown by MOCVD with NbCl_5 source [44]. Extremely high hole density $>10^{14} \text{ cm}^{-2}$ far exceeding the degenerate doping limit has been accomplished. With vapor–liquid–solid approach and NH_4VO_3 , and NaVO_3 as source precursors, uniform V-doped metallic-like monolayer MoS_2 and WSe_2 with doping density as high as $>20\%$ have been synthesized by CVD while maintaining good crystalline [43, 45].

4.1.1.2 n-Doping The elements with more valence electrons dope host TMDCs with electrons. Re is a most commonly studied n-type dopant for TMDCs, in particular for MoS_2 . First-principle calculations reveal that 1% Re substitution forms the shallow donor states at 0.1 eV below the conduction band minimum of MoS_2 [46]. TMDCs with Re-doping of 0.3–1% have been synthesized by CVD mixed with ReO_3 as source precursor [46], by liquid phase CVD with NH_4ReO_4 and NaReO_4 [47], and by MOCVD with $\text{Re}_2(\text{CO})_{10}$ [44]. Regarding the optical properties of Re-doped MoS_2 , clear blue shift in PL peak was seen with 0.3% doping [40], while others reported the opposite red shift and significantly quenched PL peaks in 1% doped MoS_2 attributed to enhanced carrier concentration [46].

4.1.1.3 Isoelectronic Doping Isoelectronic doping means replacing metal atoms using another element with equivalent valence electrons, which can suppress native defects. Thanks to the strong hybridization between p-orbitals of Se and d-orbitals of

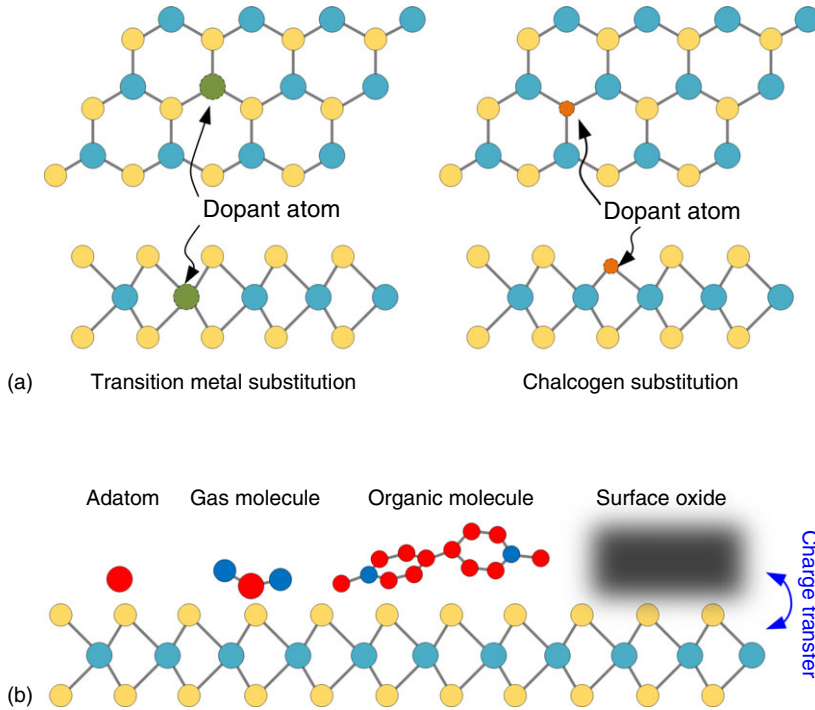


Figure 3 Schematics of (a) substitutional doped, and (b) surface charge transfer doped TMDC.

W, W-doping suppresses the formation of Se vacancies and the associated deep defect states in monolayer MoSe_2 . A 2% W-doping is able to reduce Se vacancies by 18% [48]. Subsequently, defect-related emission of PL is significantly quenched. As W has larger electron affinity than Mo, W substitution introduces p-doping to MoSe_2 .

4.1.1.4 Structural Transition Substitutions of metal atoms do not only modulate electronic and optical properties of 2D semiconductors but may also cause structural transitions due to the associated strain effect from lattice distortion. Nb doping $>0.1\%$ may lead to structural transition from 2H stacking to rhombohedral (3R) stacking in MoS_2 [49]. Re doping $>40\%$ changes MoSe_2 from 2H phase to a meta-stable $1T'$ phase [50]. Similar structural transition was noted in other doped TMDCs, such as W-doped MoTe_2 [51] and Nb-doped WSe_2 [52].

The doping with transition metal substitution provides good stability due to the

formation of new chemical bond. Nevertheless, the doping by substituting metal atoms has to be introduced at the growth state, therefore providing no opportunity to defining spatial doping profile with area selectivity.

4.1.2 Chalcogen Substitution

In addition to transition metal substitution, chalcogen atoms can also be replaced by pnictogen, chalcogen, and halogen elements, e.g. N, O, and Cl. Directly growing TMDCs with dopants could be challenging due to the high chalcogen vapor pressure in growth conditions, particularly in CVD growth. Chalcogen substitution is normally introduced by postgrowth treatments in the TMDCs prepared with intentional chalcogen vacancies. In contrast to metal substitution, chalcogen substitutional doping exhibits the possibility of area selectivity.

4.1.2.1 p-Doping p-Doping has been reported by substituting nitrogen atoms

on chalcogen vacancies by N_2 or NH_3 plasma treatments [53, 54] or by thermal annealing in NH_3 [55].

4.1.2.2 n-Doping Cl is a typical n-dopant to TMDCs, which can be introduced by a long soaking in undiluted 1,2-dichloroethane [56] or by a remote plasma treatment [57]. A shift of work function from 4.6 to 4.3 eV toward the conduction band has been measured in the plasma Cl-doped MoS_2 by Kelvin probe force microscopy, indicating an n-doping effect [57].

Although the postgrowth chalcogen substitution is able to selectively dope the designated areas, chemical and plasma processes inevitably generate defects in the 2D lattice defects, leading to performance degradation.

4.1.2.3 Isoelectronic Doping Isoelectronic doping by group 16 elements can passivate pristine chalcogen vacancies. As substitutions usually occur on the surface by plasma or chemical treatments, they are not able to passivate the bulk defects for few-layer TMDCs. Controlled low-pressure oxygen annealing has been developed to induce oxygen intercalation between the layers in MoTe_2 [58]. Due to the very different activation energies at defect sites and intrinsic MoTe_2 , intercalated oxygen only selectively occupies Te vacancies to remove charged states without oxidizing MoTe_2 . Consequently, this leads to the passivation of Te-vacancies to restore the electronic properties for MoTe_2 .

4.2 Surface Charge Transfer Doping

Owing to their ultra-thin nature, 2D semiconductors are extremely sensitive to surrounding environments. Surface adsorptions and modifications, as illustrated in Figure 3b, can controllably dope underlying 2D semiconductors through charge transfer determined by their work function, electron affinity, and concentration. Surface charge transfer doping is known as an efficient and

non-destructive doping strategy for 2D semiconductors beyond traditional substitutional doping. Charge transfer doping fundamentally relies on physical adsorption, therefore, it is less stable than the doping by chemical bonding. Air stability is a serious concern to develop surface charge transfer doping techniques.

4.2.1 Surface Adsorption

Upon air exposure, gas molecules inevitably adsorb on the surface of 2D semiconductors, therefore causing doping effect. Oxygen and moisture are the typical p-dopants to most of the 2D semiconductors. Their adsorption dramatically enhances the PL intensity in n-type MoS_2 and MoSe_2 due to the depletion of electrons, whereas it degrades the PL intensity in the p-type WSe_2 [59]. K can be controllably decorated on surface by exposing 2D semiconductors to K vapor, which has extremely low work function of 2.3 eV and acts as an n-dopant. High electron concentrations of $1 \times 10^{13} \text{ cm}^{-2}$ and $2.5 \times 10^{12} \text{ cm}^{-2}$ have been obtained in K-doped MoS_2 and WSe_2 , respectively, reaching the degenerate doping limit [60]. AuCl_3 is one of the most common p-type dopants for 2D semiconductors [61, 62], which transforms into Au particles by accepting electrons from semiconductors. Nevertheless, these doping effects are not stable in air.

4.2.2 Organic Molecules

Organic molecules can be easily applied on the surface of 2D semiconductors by spin-coating or drop-casting, showing the advantages of low-cost and large area coverage. Benzyl viologen (BV) is known as an air-stable n-dopant to TMDCs. Degenerate electron density of $1.2 \times 10^{13} \text{ cm}^{-2}$ was obtained in BV-doped MoS_2 in air [63]. Other reported air-stable molecular dopants for TMDCs are listed below. The n-dopants include triphenylphosphine (PPh₃) [64], diethylenetriamine (DETA) [65], and tetrathiafulvalene (TFF) [66]. The p-dopants include 4-nitrobenzenediazonium (4-NBD) [65], tetracyanoethylene (TCNE) [67], and

tetrafluoro-tetracyanoquinodimethane (F4-TCNQ) [68]. Similar to the issue of chemical passivation mentioned earlier, uniformity remains a problem of molecular process.

4.2.3 Surface Oxidation

Native oxides of molybdenum and tungsten chalcogenides, i.e. MoO_x and WO_x ($x \leq 3$), possess high work functions of 6.6 and 6.3 eV, respectively, which induce effective p-doping to the related TMDCs. Self-limiting oxidation has been reported in WSe_2 and MoTe_2 by low-power oxygen plasma and ozone treatments [69, 70]. By the process, only the topmost layer can be oxidized, which prevents underlying semiconducting layers from the formation of defects. In comparison, the plasma-induced oxidation produces much stable p-doping characteristics than the ozone treatment. Robust degenerate p-doping with the hole concentration of $1.0 \times 10^{13} \text{ cm}^{-2}$ and $2.5 \times 10^{13} \text{ cm}^{-2}$ has been demonstrated, respectively, in the intrinsic n-type WSe_2 and MoTe_2 by plasma treatment [71, 72]. The doping concentration almost remains after a long-term storage in air and soaking in organic solutions. Using capping masks, selective doping can be realized to define various device functions such as p–n junctions. The plasma treatment is also compatible to the conventional thin film technology, making them promising for building 2D electronics and optoelectronics.

5 Contact Engineering

5.1 Contact Related Issues

Electric contact is of great importance in terms of the electronic and optoelectronic devices. When a metal is contacted to a semiconductor, a Schottky barrier forms at the interface due to the mismatch in the Fermi levels of both materials, giving rise to the contact resistance. In addition, the so-called Fermi level pinning (FLP) effect may take place at the contact interface,

by which the Fermi level is pinned inside the energy band gap regardless of contact metals.

In terms of conventional bulk semiconductors, e.g. silicon, the contact regions are degenerately doped to achieve the Ohmic contact and low contact resistance. The contact resistance can also be lowered with the heavily doped 2D semiconductor by implementing surface charge transfer doping. N-type and p-type ohmic contacts with low contact resistance of ~ 1 and $2.3 \text{ k}\Omega \cdot \mu\text{m}$ were reported for MoS_2 by using AuCl_3 and BV as dopants, respectively [62, 63]. Low contact resistance of $0.6 \text{ k}\Omega \cdot \mu\text{m}$ was achieved on the degenerately doped MoTe_2 by surface oxide MoO_x [72]. However, as mentioned earlier, the stable degenerate doping is still a technical challenge for 2D semiconductors.

High contact resistance in the range of $10\text{--}10^4 \text{ k}\Omega \cdot \mu\text{m}$ has been frequently measured in TMDCs based devices with deposited metal contacts, which is far larger than the requirement of $0.1 \text{ k}\Omega \cdot \mu\text{m}$ for ultimate performance, and is acting as one of the roadblocks of 2D electronic and optoelectronic devices. Under this circumstance, contact resistance can be orders of magnitude larger than channel resistance. Subsequently, on-state current and device switching are predominated by contact instead of semiconductor channel, hindering the applications with high power consumption and low on-state current. Secondly, the effective field effect mobility is also suppressed owing to the poor contact. Another issue associated with the strong FLP is the unadjustable polarity characteristics in TMDCs based 2D devices. N-type characteristic has always been measured for MoS_2 regardless of the contact metals. With MoTe_2 and WSe_2 , n-type or electron-dominant ambipolar behaviors have usually been reported. Such feature is unfavorable for realizing the concept of 2D complementary logic devices and circuits, which require the electric devices with both n-type and p-type polarities.

5.2 Origins of Fermi Level Pinning

5.2.1 Metal-Induced Gap States

When a metal is contacted on semiconductor, the wave function of valence electrons in the semiconductor needs to be overlapped with that of valence electrons in the metal at the interface. Since the Fermi levels of the metal and semiconductor must align to each other at the interface, metal-induced gap states (MIGS), therefore, exist and decay deeper into the semiconductor, which intrinsically contribute to FLP. MIGS also plays an important role in the FLP of 2D semiconductors but are much more complex than that in bulk semiconductors. It is known that the d-orbitals of the contact metal and p-orbitals of TMDCs are strongly hybridized. The orbital overlap states significantly distort the properties of 2D semiconductors, leading to considerable FLP.

Atomic-level simulation is required to investigate the situation at the interface for each individual 2D semiconductor–metal junction [73]. According to the different strength of hybridization, the contact is described by three different models:

- (i) With negligible hybridization, the vdW gap at the contact interface behaves as a tunnel barrier and contributes to the contact resistance.
- (ii) With intermedium hybridization, the vdW gap vanishes, and overlaps states emerge and causes severe FLP.
- (iii) In an extreme case, the contact metal is strongly bonded to the 2D semiconductor by forming covalent bonds.

5.2.2 Interface Dipole

In addition to MIGS, interface dipole originated from the interface charge redistribution and also contributes to FLP by modifying interfacial band alignment. Interface dipole-induced FLP is a unique feature of 2D semiconductors, which is negligible in bulk semiconductors. It is worth noting that interface dipole can be utilized to realize Ohmic contact to 2D semiconductors with extremely low contact resistance. Bismuth

is a semimetal with the work function close to the conduction band minimum of MoS_2 , WS_2 , and WSe_2 and a near-zero density of state at the Fermi level, greatly suppressing conduction band contributed MIGS [74]. Due to the formation of interface dipole, bismuth strongly n-dopes MoS_2 to the degenerate state of $1.5 \times 10^{13} \text{ cm}^{-2}$, which pins the Fermi level of MoS_2 inside the conduction band, leading to vanished electron Schottky barrier height (SBH) and an ultra-low contact resistance of $0.123 \text{ k}\Omega\cdot\mu\text{m}$.

5.2.3 Disorder-Induced Gap States

Various disorders are created in 2D semiconductors especially on the surface during growth or by the fabrication process. Disorders are hard to be excluded from 2D devices, especially deposited metal is employed for contact. Empty states can be occupied and move inside the band gap forming disorder-induced gap states (DIGS), which contribute to FLP at the defect sites. In most of the reported 2D devices, the FLP is a mixed effect of MIGS and DIGS. Spatially resolved SBH maps measured by conductive atomic force microscopy reveal a reduction of 30–40% in the pinning factor, which measures the dependence of the SBH on work function of contact metal, for the defective regions compared to the intrinsic surface for MoS_2 , MoTe_2 , WSe_2 , WS_2 [75, 76].

5.3 Contact Strategies

Considering the strong FLP and the unique features of 2D semiconductors, several contact techniques have been developed to reduce the contact resistance for 2D devices.

5.3.1 vdW Contacts

The vdW contact that is mechanically transferred onto 2D semiconductors is developed to eliminate DIGS caused by metal deposition. Prepatterned metal contacts can be picked up from a substrate using a poly(methyl methacrylate)/polydimethylsiloxane (PDMS/PMMA)

stamp with the assistance of hexamethyldisilane, then transferred onto 2D semiconductors forming atomically flat and nearly damage-free vdW contact interface [77]. The schematic of a Gr contacted TMDC is illustrated in Figure 4a. High pinning factor approaching 1 has been reported for the 2D semiconductors with transferred metal contacts, indicating the fully suppressed FLP. Therefore, polarity of the devices is controllable from n-type to p-type with contact metals of varied work functions. Besides metals, 2D materials such as Gr, metallic TMDCs, and MXene can be used as FLP-free vdW contacts to 2D semiconductors [78].

5.3.2 Contacts with Inserting Layer

Inserting a thin insulating tunnel barrier between contact metal and 2D semiconductors can suppress the interfacial interactions, including both orbital hybridization and dipole, therefore weakening FLP and improving contact conditions. Insulating oxides such as ZnO, TiO₂, and Ta₂O₅ can be introduced as the inserting layer. However, the inserting layer adds energy barrier at the contact interface and extra tunneling process in carrier injection. Experiments found that an oxide layer thinner than 2 nm is required to achieve improved contact quality. A 1-nm-thick TiO₂ inserting layer can increase the pinning factor from 0.02 to 0.24 for MoS₂ [79]. Growth of the oxide layer on 2D semiconductors is technically challenging. Monolayer h-BN can be used alternatively as the inserting layer [80]. Figure 4b illustrates the schematic of a metal contacted TMDC with monolayer h-BN as inserting layer. However, contact with inserting layer host an area-dependent carrier injection, which is not favorable for the highly scaled device [81].

5.3.3 Edge Contact

One-dimensional contact can be formed to the edges of 2D semiconductors following a complex fabrication procedure. 2D semiconductor is firstly capped by h-BN or photoresist. Then the edges are exposed by

controlled plasma etching before metal deposition. The schematic of the TMDC with edge contact is illustrated in Figure 4c. Etched edges possess numerous dangling bonds. Subsequently, covalent bonds are formed between contact metal and 2D semiconductors to facilitate effective carrier injection. It is worth mentioning that no significant FLP emerges due to the low dimensionality of the 1D contact interface. Hence, the polarity of transistor device is controllable by changing the edge contact metals with varied work functions [82]. However, large contact resistance of 10–100 kΩ·μm was often reported for the edge-contact TMDC devices [83, 84].

5.3.4 Seamless Contact by Phase Transition

Area selective phase transition can be implemented by converting parts of the 2D semiconductors into metallic phase as the seamless electric contacts [85]. Figure 4d illustrates the metallic 1T phase TMDC as the seamless contact to the semiconducting 2H part by phase transition. Contacting on the metallic 1T phase of monolayer MoS₂ achieved by *n*-butyl lithium chemical treatment gives a low contact resistance of 0.24 kΩ·μm, which is five times improved compared to the contacts on 2H semiconducting MoS₂ [86]. Laser-induced phase transition in MoTe₂ has been utilized to realize the seamless ohmic contact for MoTe₂ with a negligible SBH of 10 meV [87].

6 Photodetectors

Compared to conventional 3D bulky semiconductors, 2D semiconducting materials possess novel photonic and optoelectronic properties which make them as promising materials for applications such as photodetectors. For example, the quantum confinement along the out-of-plane direction leads novel light–matter interactions that are distinctively different from the bulky counterparts [4, 21, 88, 89]. The self-terminated (or self-passivated) surface is free of dangling bonds, which enables an

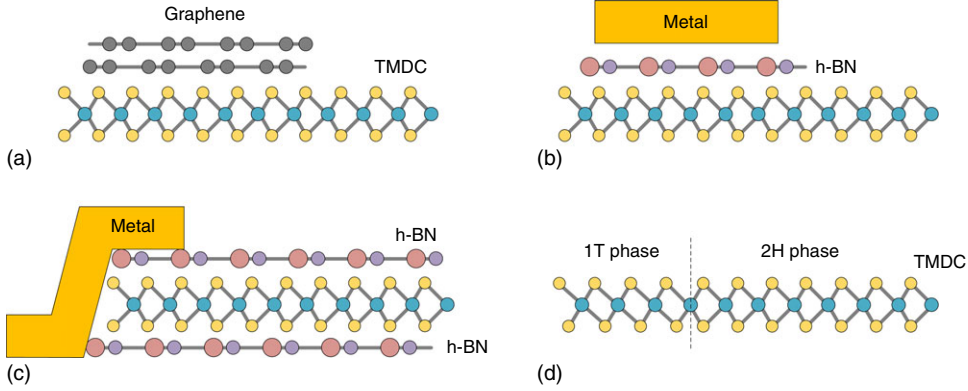


Figure 4 Schematics of the TMDC flake with (a) vdW contact, (b) contact with inserting layer, (c) edge contact, and (d) seamless contact by phase transition.

ultrafast charge separation and transfer at atomically sharp junction interfaces without the conventional lattice mismatch issue [90–92]. In addition to the high-efficiency and broad-spectrum optical absorption, the mechanical bendability and stretchability of 2D semiconductors provide unique advantages for flexible devices such as wearable sensors [93]. Here, we emphasize on the photodetector applications based on 2D semiconductors, and summarize the physical mechanisms, performance metrics, and state-of-the-art benchmarks.

6.1 Mechanisms of Photocurrent Generation

The operation of photodetectors is relying on a variety of light-induced physical

phenomena, as shown in Figure 5. In general, these mechanisms can be classified according to the nature of the physical effects caused by the incident radiation. Optoelectronic detectors rely on electron–hole pairs produced directly by light excitation, and possess advantages in terms of signal-to-noise ratio (SNR) and fast response. Photothermoelectric (PTE) detectors involve the changes in electron or lattice temperature which is induced by the absorbed radiation and indirectly leading to a measurable change in the physical quantity of electrical detection. Here, we briefly review a few representative mechanisms based on the optoelectronic and PTE detection, and benchmark the performance metrics of photodetectors using 2D semiconductors.

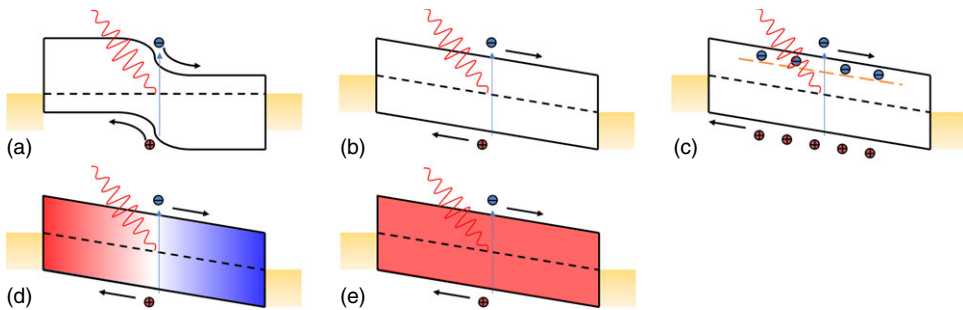


Figure 5 Energy band diagram and schematic illustration indicate a variety of photodetection mechanisms, include (a) photovoltaic effect, (b) photoconductive effect, (c) photogating effect, (d) photothermoelectric effect, and (e) photobolometric effect.

6.1.1 Photovoltaic Effect

A photovoltaic (PV) effect generates photocurrent in a junction structure of 2D semiconductors, for example, a homogeneous or heterogeneous p–n junction or a metal–semiconductor junction [94, 95]. Specifically, the electron–hole pairs are generated under light, separated under an electric field, and consequently contribute to the formation of a voltage across the junction. The initial built-in electric field within the junction structure drives the electron–hole pair separation to a limited extent. Therefore, other technologies such as surface chemical modification of 2D semiconductors and asymmetric source–drain metallization can also enlarge the built-in electric field and benefit the higher built-in electric field generation. Especially for 2D materials, the vdW layer structure can provide an atomically clean and sharp junction interface, for example, a $\text{WSe}_2/\text{MoS}_2$ heterojunction [96]. Compared to the conventional bulky structures, the vdW layer structure also possesses a significantly shortened transmission distance along the out-of-plane direction, and consequently facilitates the charge carrier transport and collection [97].

6.1.2 Photoconductive Effect

Under the photoconductive (PC) effect, the photo-induced additional carriers lead to an increase in the free carrier concentration and thus a decrease in the resistance of the semiconductor [98, 99]. The excess carriers are separated by the applied bias voltage, resulting in a photocurrent generation. In dark conditions, the finite carriers are driven by the applied voltage and can produce a small dark current. Under illumination, with the additional photocurrent, the current becomes more significant than the dark current. Compared to the PV effect (light-induced generation of voltage) which occurs without an external voltage or electric field, the PC effect (light-induced generation of current) requires the external voltage or electric field to drive the carriers and form the photocurrent.

6.1.3 Photogating Effect

The photogating (PG) effect is a particular case of the PC effect [100–102]. The PG effect serves as an additional gating approach to modulate the conductivity under the light illumination. Specifically, the electrons or holes are generated by photo excitation. If the carriers are captured by the traps (for example, defects or interfacial states from a SiO_2 substrate), the charged trap state can act as a local floating gate and modulate the channel conductance. Taking a positively charged hole trap state as an example, it will lead to an electron doping and thus a shift of transfer characteristics toward the negative gate voltage direction. For 2D semiconductors, the PG effect can create a remarkable photoresponse, so an integration with a high density of charge traps can promote the PG effect [102–104].

6.1.4 Photothermoelectric Effect

The PTE effect is caused by the light-induced temperature difference, which can cause thermal voltage and play an essential role in the light response generation of many photosensitive 2D semiconductor devices [105–107]. Under light illuminations, hot carriers transfer energy slowly to the crystal lattice in the semiconductor and form a hot fermion distribution. In the photodetector operation without external voltages, the generation of photocurrent is related to both the PV and PTE effects. Because the directions of the photocurrent caused by the PTE and PV effects are the same, two mechanisms are easily confused. Taking MoS_2 as an example, it is demonstrated that the PTE effect is dominant mechanism for the photocurrent generation in monolayer MoS_2 , instead of the conventional understanding of the PV effect occurring at the metal–semiconductor interfaces [108]. Whereas for the multilayer MoS_2 , the presence of both the PV and PTE effects has also been identified [109].

6.1.5 Photobolometric Effect

The bolometer detector based on photobolometric (PB) effect is mainly made of

semiconductor or superconductor absorbing material, is widely used in the submillimeter wave (THz) band [110, 111], and is one of the most sensitive detectors. The bolometric effect is related to the direct heating of the 2D semiconductor by the incident photons, resulting in the change of the carrier mobility of the 2D semiconductor [112]. Since this photodetection mechanism is based on light-induced conductance changes rather than direct photocurrent generation, it requires an external bias. An appropriate gate voltage can facilitate the radiant heat effect and significantly improve the responsivity of the PB effect. For example, it has been reported that a MoS₂ photo transistor exhibited a negative photocurrent in infrared regime in which the PB effect caused lattice heating and thus increases resistance [113]. For the case of ReS₂, the negative photoresponse can be further switched to a positive one by applying the gate voltage and exploited for ultralow optical power detection in visible regime [114].

6.2 Characterizations of 2D Photodetectors

To better compare the performance of photodetectors of different sizes and under different operating conditions, we summarize a list of key metrics commonly used to describe the performance of photodetectors, including responsivity, quantum efficiency, SNR, bandwidth, and detection capability. We also collect some representative 2D photodetectors based on 2D homogeneous materials and 2D vdW heterostructures, as listed in Table 1.

6.2.1 Responsivity (R)

The ratio of the photocurrent (I_p) magnitude to the incident photo power (P) is defined as the spectral responsivity and expressed as:

$$R = \frac{I_p}{P} = \frac{I_{\text{light}} - I_{\text{dark}}}{P}$$

where I_{light} and I_{dark} are the currents measured in the illuminated and dark

environment, respectively. In general, the responsivity varies with the incident optical power, wavelength, and the applied electric field. Commercially available Si-based photodiodes can reach 500 mA W⁻¹ at the sensing wavelength of 405–1100 nm. As a comparison, a MoSe₂ phototransistor can provide highest photoresponsivity of 242 A W⁻¹ [129], and a lateral MoS₂/WS₂ heterojunctions photodetectors can boost it further up to 567.6 A W⁻¹ [130], indicating the promising potential of 2D materials for next-generation phototransistors.

6.2.2 External Quantum Efficiency (EQE)

When the phototransistor operates based on the PV effect, not all the incident photons can be absorbed to generate electron–hole pairs. Even though the electron–hole pairs are generated, some of them cannot contribute to the photocurrent due to recombination or capture processes. Therefore, external quantum efficiency (EQE) is defined as:

$$\text{EQE} = \frac{I_p/e}{P/h\nu} = R \frac{hc}{e\lambda}$$

where e is the electron charge, h is the Planck constant, c is the speed of light, λ is the wavelength of light, and ν is the frequency of light. Due to the low light absorption efficiency of the monolayer 2D semiconductor, a higher EQE can be achieved by increasing the thickness of the material to improve the light absorption efficiency and reduce the recombination of photogenerated carriers.

6.2.3 Internal Quantum Efficiency (IQE)

In a comparison with EQE, internal quantum efficiency (IQE) is the ratio of the number of electron–hole pairs produced to the number of photons absorbed, which is rewritten as:

$$\text{IQE} = \frac{\text{EQE}}{\text{total photon absorption}}$$

In general, IQE is always greater than EQE because refraction and transmission cannot be eliminated. Also, if the material is extremely thin, the interference effect of light needs to be considered.

Table 1 Performance of 2D semiconductor photodetectors.

Mechanism	Active materials	Spectral range	Responsivity	Detectivity	References
Photovoltaic (PV)	WSe ₂	532 nm	2.31 A W ⁻¹	9.16 × 10 ¹¹ Jones	[115]
	MoS ₂ /WS ₂	532 nm	4.36 mA W ⁻¹	4.36 × 10 ¹³ Jones	[116]
	SnS ₂	515 nm	2.3 × 10 ³ A W ⁻¹	3.2 × 10 ¹² Jones	[117]
	MoTe ₂	1500 nm	0.5 A W ⁻¹	6.92 × 10 ⁹ Jones	[118]
Photoconductive (PC)	MoSe ₂	670–1458 nm	10.1 A W ⁻¹		[119]
Photogating (PG)	MoS ₂	550 nm	10 ⁵ A W ⁻¹	10 ¹⁴ Jones	[120]
	PdSe ₂	1.06 μm	708 A W ⁻¹	1.31 × 10 ⁹ Jones	[121]
	MoS ₂	637 nm	96.8 A W ⁻¹	4.75 × 10 ¹⁴ Jones	[122]
	p-MoS ₂ /n-MoS ₂	640–800 nm	7 × 10 ⁴ A W ⁻¹	3.5 × 10 ¹⁴ Jones	[123]
	WSe ₂ /MoS ₂	450–800 nm	2700 A W ⁻¹	5 × 10 ¹¹ Jones	[124]
Photothermoelectric (PTE)	Monolayer MoS ₂	532 nm	430 A W ⁻¹	10 ¹¹ Jones	[125]
	T _d -MoTe ₂	532 nm–10.6 μm	0.40 mA W ⁻¹	1.07 × 10 ⁸ Jones	[126]
	PdSe ₂	532 nm	1.3 mA W ⁻¹	2.55 × 10 ⁷ Jones	[127]
Photobolometric (PB)	MoS ₂	980–1550 nm	1.9 × 10 ⁴ A W ⁻¹		[113]
	SnSe	1550–10 600 nm	0.16 A W ⁻¹	3.9 × 10 ⁷ Jones	[128]
	ReS ₂	1200 nm	350 A W ⁻¹	1.3 × 10 ¹⁰ Jones	[114]

6.2.4 Photogain (G)

G represents the number of photoexcited electron–hole pairs per single incident photon, which can be expressed as:

$$G = \frac{I_p}{e\Delta nA}$$

where Δn is the number of photoexcited charge carriers, and A is the active channel area. From a microscope perspective, it can be considered as the ratio of the lifetime of the photoexcited charge carriers (τ_c) to the time required for charge carrier transport along the channel (τ_t). For the given material, device structure, biasing condition, G can be written as

$$G = \frac{\tau_c}{\tau_t} = \frac{\tau_c \mu V}{L^2}$$

where μ is the charge carrier mobility, V is the applied voltage along the channel, and L is the channel length. By combining high carrier mobility of Gr and high photoresponsivity of MoS₂, a MoS₂/Gr heterojunction photodetector has been demonstrated with an ultrahigh G greater than 10⁸ [131].

6.2.5 Response Time (τ) and Bandwidth (B)

Response time of the photodetector reflects the ability of detecting a rapidly modulated light signal. It includes the rise time τ_r and the fall time τ_f which are the time required for the peak current of the device to flow from 10% to 90% and the time required for the peak current of the device to flow from 90% to 10%, respectively. Commercially available Si photodiodes typically have a rise time of 50 ps, while Gr photodetectors can have a response time of several hundred picoseconds. Other 2D materials still require further investigation and engineering efforts to improve the response time. For example, a four-layer MoTe₂ photodetectors have a rise time of 160 μs and fall time of 300 μs [132]. Au–WS₂–Au asymmetric bottom-contacted photodetector shows a fast rise time of 7 ms and fall time of 37.2 ms [133]. A MoS₂/p-Si heterojunction photodetector with asymmetric electrodes shows a photoresponse/recovery time of 74 ms/115 ms [134].

Conductivity and photoconductivity usually change the response time of the photodetector. Due to the trap states, the attenuation of the photocurrent is also strongly dependent on the intensity of the light incident on the device. The longer response time may be attributed to the low conductivity and traps in the 2D semiconductor film. Since the trap density, trap energy distribution, and carrier capture probability may be different, more complex mechanisms are at play and deserve further investigation. For most optoelectronic devices, the optical responsivity depends on the optical modulation frequency (f) and is expressed as:

$$R(f) = \frac{R_0}{\sqrt{1 + (2\pi f\tau)^2}}$$

where R_0 is photoresponsivity measured under static illumination. As f increases, R decreases. The modulation frequency where the optical responsivity decreases to -3 dB is called bandwidth, also known as the cutoff frequency. The broadband photodetectors are needed for high-speed information transmission, and graphene photodetectors can have a bandwidth of about tens of GHz.

6.2.6 Signal-to-Noise Ratio (SNR)

Since noise produces random fluctuations in the output of the detector signal, the presence of noise in the detection process can have an impact on the detection of the signal. SNR is given as:

$$\text{SNR} = \frac{\text{Signal power}}{\text{Noise power}}$$

The signal power can be detected only when it is higher than the noise power, i.e. $\text{SNR} > 1$.

6.2.7 Noise Equivalent Power (NEP)

Noise equivalent power (NEP) is the minimum optical signal power that an optical detector can detect or distinguish from the total noise. It is defined as the optical input power required to achieve an SNR of 1 at a

bandwidth of 1 Hz and can be expressed as:

$$\text{NEP} = \frac{P}{\sqrt{B}}$$

where P is the incident power that results in $\text{SNR} = 1$. NEP in commercially available silicon photodiodes can reach $10^{-14} \text{ W (Hz}^{-1/2})^{-1}$, whereas it is about $1.22 \times 10^{-13} \text{ W (Hz}^{-1/2})^{-1}$ in a 2D GeSe/MoSe₂ heterojunction diode [135]. A photodetector made from an exfoliated 10-nm-thick BP has shown NEP value of 40 nW $(\text{Hz}^{-1/2})^{-1}$ [136].

6.2.8 Detectivity (D^*)

To better compare the performance between different detectors, the effects of bandwidth, geometry, and device area should be considered. The detectivity reflects the sensitivity of the photodetector, and it takes into account the NEP, area, and bandwidth as:

$$D^* = \frac{(AB)^{\frac{1}{2}}}{\text{NEP}}$$

where A is the photosensitive area. If the dark current of the device is much larger than the noise, the detectivity can be further expressed as:

$$D^* = \frac{RA^{\frac{1}{2}}}{(2eI_{\text{dark}})^{\frac{1}{2}}}$$

A higher detectivity indicates better detection performance of the photodetector, which can be improved by increasing the response rate, increasing the detection area, and reducing the dark current of the device. The detectivity of silicon photodiodes is about 10^{12} Jones, while 2D semiconductors can reach 10^{16} Jones by combining with quantum dots to form a hybrid structure.

7 Summary and Perspective

The photodetectors based on 2D semiconductors have demonstrated their promising potential for next-generation high-performance optoelectronics application. Yet, there are still challenges and issues

which need to be further addressed. Here we only list a few examples.

First, the response time of 2D photodetectors needs to be improved. Graphene as a 2D semi-metal possesses outstanding carrier mobility ($\sim 200\,000\text{ cm}^2\text{ (Vs)}^{-1}$) [137, 138] and thus ultrafast response in photodetection (response time in 2.1 ps, frequency over 100 GHz) [139, 140]. Owing to the bandgap, the carrier mobility in 2D semiconductors is significantly reduced ($\sim 1000\text{ cm}^2\text{ (Vs)}^{-1}$ for monolayer MoS_2) [141], and consequently impacts the response time (from 10 ms to 10 s) [142]. To overcome this issue, a synergistic combination of both graphene and 2D semiconductors in device design can be a promising approach that can merge their own advantages and create high-performance photodetectors [131, 143].

Second, the abovementioned definitions of NEP and specific detectivity are based on a simple assumption that the shot noise is the primary noise source in the photodetectors [144]. For a more practical case, the impacts of thermal and flicker noises need to be considered. The shot noise limit is typically valid for heterojunction-based photodetectors, but usually invalid for PC detectors. Moreover, the flicker noise contribution to 2D semiconductors-based photodetectors were also widely reported as the main noise source. In such cases, many of the prior work may have overestimated/overclaimed the performance of NEP and specific detectivity [145]. Third, with the promising potential for further high-performance photodetectors, there are still challenges and issues with 2D materials. As listed in Table 1, the superior performance of 2D photodetectors based TMD semiconductors has been demonstrated. One can foresee that, with the natural advantage in mechanical flexibility, 2D semiconductors such as TMDs will be an outstanding material candidate, in principle, to replace the conventional bulky and rigid 3D semiconductors. The current flexible electronics and optoelectronics rely on the organic semiconductors, which suffer from low carrier mobility and innegligible thermal

instability. Thanks to the combination of high carrier mobility, excellent flexibility, and environmental stability, an opportunity for 2D semiconductors may emerge in the flexible optoelectronics [93]. However, one should also note that most of adopted 2D materials were just random-distributed, irregular-shaped, micron-size flakes prepared by mechanically exfoliation with tapes. The extremely low yield, reproducibility, and consequently performance-to-cost ratio make them impractical for mass-production commercialization with standard semiconductor processing. The exact dopants and doping concentration in 2D semiconductors remain poorly defined and demand more fundamental investigations. Additionally, the conventional dielectric or metal integration approaches used in silicon electronics are often too aggressive and can damage delicate 2D channels [146]. It is more rational to take the advantage of mature silicon technology and develop a possible approach to integrate 2D materials with existing semiconductor manufacturing processes, especially in material synthesis and device fabrication [147].

Acknowledgments

Jian Sun acknowledges support from the Hunan High-Level Talent Program (Grant No. 2019RS1006). Cheng Yang acknowledges support from the National Natural Science Foundation of China (11874244 and 11974222). Fei Yao and Huamin Li thank Yu Fu and Hemendra N. Jaiswal for discussions.

Related Articles

Photodetectors*
Photovoltaic Devices
Optoelectronics
Transistors, Field-effect
Thin Films, Electrical Properties

References

- 1 Novoselov, K.S., Geim, A.K., Morozov, S.V. et al. (2004). *Science* 306 (5696): 666–669.
- 2 Mas-Ballesté, R., Gómez-Navarro, C., Gómez-Herrero, J., and Zamora, F. (2011). *Nanoscale* 3 (1): 20–30.
- 3 Wang, Q.H., Kalantar-Zadeh, K., Kis, A. et al. (2012). *Nat. Nanotechnol.* 7 (11): 699–712.
- 4 Xia, F., Wang, H., Xiao, D. et al. (2014). *Nat. Photonics* 8 (12): 899–907.
- 5 Roldán, R., Chirolli, L., Prada, E. et al. (2017). *Chem. Soc. Rev.* 46 (15): 4387–4399.
- 6 Rasmussen, F.A. and Thygesen, K.S. (2015). *J. Phys. Chem. C* 119 (23): 13169–13183.
- 7 Tang, L., Tan, J., Nong, H. et al. (2021). *Acc. Mater. Res.* 2 (1): 36–47.
- 8 Liu, Y., Huang, Y., and Duan, X. (2019). *Nature* 567 (7748): 323–333.
- 9 Chhowalla, M., Jena, D., and Zhang, H. (2016). *Nat. Rev. Mater.* 1 (11): 1–15.
- 10 Liu, B., Abbas, A., and Zhou, C. (2017). *Adv. Electron. Mater.* 3 (7): 1700045.
- 11 Kang, S., Lee, D., Kim, J. et al. (2020). *2D Mater.* 7 (2): 022003.
- 12 Li, W., Qian, X., and Li, J. (2021). *Nat. Rev. Mater.* 6 (9): 829–846.
- 13 Nourbakhsh, A., Zubair, A., Sajjad, R.N. et al. (2016). *Nano Lett.* 16 (12): 7798–7806.
- 14 Yoon, Y., Ganapathi, K., and Salahuddin, S. (2011). *Nano Lett.* 11 (9): 3768–3773.
- 15 Liu, L., Kumar, S.B., Ouyang, Y., and Guo, J. (2011). *IEEE Trans. Electron Devices* 58 (9): 3042–3047.
- 16 English, C.D., Smithe, K.K.H., Xu, R.L., and Pop, E. (2016). Approaching ballistic transport in monolayer MoS₂ transistors with self-aligned 10 nm top gates. *2016 IEEE International Electron Devices Meeting (IEDM)*. pp. 5.6.1–5.6.4.
- 17 Desai, S.B., Madhvapathy, S.R., Sachid, A.B. et al. (2016). *Science* 354 (6308): 99–102.
- 18 Liu, L., Kong, L., Li, Q. et al. (2021). *Nat. Electron.* 4 (5): 342–347.
- 19 Bernardi, M., Palummo, M., and Grossman, J.C. (2013). *Nano Lett.* 13 (8): 3664–3670.
- 20 Tsai, M.-L., Su, S.-H., Chang, J.-K. et al. (2014). *ACS Nano* 8 (8): 8317–8322.
- 21 Splendiani, A., Sun, L., Zhang, Y. et al. (2010). *Nano Lett.* 10 (4): 1271–1275.
- 22 Pető, J., Dobrik, G., Kukucska, G. et al. (2019). *NPJ 2D Mater. Appl.* 3 (1): 1–6.
- 23 Ryou, J., Kim, Y.-S., Kc, S., and Cho, K. (2016). *Sci. Rep.* 6 (1): 29184.
- 24 Nayak, A.P., Pandey, T., Voiry, D. et al. (2015). *Nano Lett.* 15 (1): 346–353.
- 25 Liu, Y., Qiu, Z., Carvalho, A. et al. (2017). *Nano Lett.* 17 (3): 1970–1977.
- 26 Kutana, A., Penev, E.S., and Yakobson, B.I. (2014). *Nanoscale* 6 (11): 5820–5825.
- 27 Manzeli, S., Ovchinnikov, D., Pasquier, D. et al. (2017). *Nat. Rev. Mater.* 2 (8): 1–15.
- 28 Li, X.-L., Han, W.-P., Wu, J.-B. et al. (2017). *Adv. Funct. Mater.* 27 (19): 1604468.
- 29 Peng, Z., Chen, X., Fan, Y. et al. (2020). *Light Sci. Appl.* 9 (1): 190.
- 30 Shi, H., Pan, H., Zhang, Y.-W., and Yakobson, B.I. (2013). *Phys. Rev. B* 87 (15): 155304.
- 31 Scalise, E., Houssa, M., Pourtois, G. et al. (2012). *Nano Res.* 5 (1): 43–48.
- 32 Castellanos-Gomez, A., Roldán, R., Cappelluti, E. et al. (2013). *Nano Lett.* 13 (11): 5361–5366.
- 33 Nayak, A.P., Bhattacharyya, S., Zhu, J. et al. (2014). *Nat. Commun.* 5 (1): 3731.
- 34 Fu, L., Wan, Y., Tang, N. et al. *Sci. Adv.* 3 (11): e1700162.
- 35 Qiu, Z., Trushin, M., Fang, H. et al. *Sci. Adv.* 5 (7): eaaw2347.
- 36 Chaves, A., Azadani, J.G., Als Salman, H. et al. (2020). *NPJ 2D Mater. Appl.* 4 (1): 1–21.
- 37 Song, J.-G., Ryu, G.H., Lee, S.J. et al. (2015). *Nat. Commun.* 6 (1): 7817.

- 38 Yang, H., Kim, S.W., Chhowalla, M., and Lee, Y.H. (2017). *Nat. Phys.* 13 (10): 931–937.
- 39 Hu, H., Shi, Z., Khan, K. et al. (2020). *J. Mater. Chem. A* 8 (11): 5421–5441.
- 40 Gao, J., Kim, Y.D., Liang, L. et al. (2016). *Adv. Mater.* 28 (44): 9735–9743.
- 41 Li, M., Yao, J., Wu, X. et al. (2020). *ACS Appl. Mater. Interfaces* 12 (5): 6276–6282.
- 42 Suh, J., Park, T.-E., Lin, D.-Y. et al. (2014). *Nano Lett.* 14 (12): 6976–6982.
- 43 Yun, S.J., Duong, D.L., Ha, D.M. et al. (2020). *Adv. Sci.* 7 (9): 1903076.
- 44 Gao, H., Suh, J., Cao, M.C. et al. (2020). *Nano Lett.* 20 (6): 4095–4101.
- 45 Li, S., Hong, J., Gao, B. et al. (2021). *Adv. Sci.* 8 (11): 2004438.
- 46 Zhang, K., Bersch, B.M., Joshi, J. et al. (2018). *Adv. Funct. Mater.* 28 (16): 1706950.
- 47 Zhang, T., Fujisawa, K., Zhang, F. et al. (2020). *ACS Nano* 14 (4): 4326–4335.
- 48 Li, X., Poretzky, A.A., Sang, X. et al. (2017). *Adv. Funct. Mater.* 27 (19): 1603850.
- 49 Suh, J., Tan, T.L., Zhao, W. et al. (2018). *Nat. Commun.* 9 (1): 199.
- 50 Kochat, V., Apte, A., Hachtel, J.A. et al. (2017). *Adv. Mater.* 29 (43): 1703754.
- 51 Rhodes, D., Chenet, D.A., Janicek, B.E. et al. (2017). *Nano Lett.* 17 (3): 1616–1622.
- 52 Kim, A.R., Kim, Y., Nam, J. et al. (2016). *Nano Lett.* 16 (3): 1890–1895.
- 53 Azcatl, A., Qin, X., Prakash, A. et al. (2016). *Nano Lett.* 16 (9): 5437–5443.
- 54 Jin, Z., Cai, Z., Chen, X., and Wei, D. (2018). *Nano Res.* 11 (9): 4923–4930.
- 55 Yang, Q., Wang, Z., Dong, L. et al. (2019). *J. Phys. Chem. C* 123 (17): 10917–10925.
- 56 Yang, L., Majumdar, K., Liu, H. et al. (2014). *Nano Lett.* 14 (11): 6275–6280.
- 57 Kim, K.H., Kim, K.S., Ji, Y.J. et al. (2020). *J. Mater. Chem. C* 8 (5): 1846–1851.
- 58 Liu, X., Qu, D., Wang, L. et al. (2020). *Adv. Funct. Mater.* 30 (50): 2004880.
- 59 Tongay, S., Zhou, J., Ataca, C. et al. (2013). *Nano Lett.* 13 (6): 2831–2836.
- 60 Fang, H., Tosun, M., Seol, G. et al. (2013). *Nano Lett.* 13 (5): 1991–1995.
- 61 Güneş, F., Shin, H.-J., Biswas, C. et al. (2010). *ACS Nano* 4 (8): 4595–4600.
- 62 Liu, X., Qu, D., Ryu, J. et al. (2016). *Adv. Mater.* 28 (12): 2345–2351.
- 63 Kiriya, D., Tosun, M., Zhao, P. et al. (2014). *J. Am. Chem. Soc.* 136 (22): 7853–7856.
- 64 Jo, S.-H., Kang, D.-H., Shim, J. et al. (2016). *Adv. Mater.* 28 (24): 4824–4831.
- 65 Ji, H.G., Solís-Fernández, P., Yoshimura, D. et al. (2019). *Adv. Mater.* 31 (42): 1903613.
- 66 Zhang, X., Shao, Z., Zhang, X. et al. (2016). *Adv. Mater.* 28 (47): 10409–10442.
- 67 Cai, Y., Zhou, H., Zhang, G., and Zhang, Y.-W. (2016). *Chem. Mater.* 28 (23): 8611–8621.
- 68 Wang, J., Ji, Z., Yang, G. et al. (2018). *Adv. Funct. Mater.* 28 (51): 1806244.
- 69 Yamamoto, M., Dutta, S., Aikawa, S. et al. (2015). *Nano Lett.* 15 (3): 2067–2073.
- 70 Zheng, X., Wei, Y., Deng, C. et al. (2018). *ACS Appl. Mater. Interfaces* 10 (36): 30045–30050.
- 71 Liu, X., Pan, Y., Yang, J. et al. (2021). *Appl. Phys. Lett.* 118 (23): 233101.
- 72 Liu, X., Qu, D., Yuan, Y. et al. (2020). *ACS Appl. Mater. Interfaces* 12 (23): 26586–26592.
- 73 Kang, J., Liu, W., Sarkar, D. et al. (2014). *Phys. Rev. X* 4 (3): 031005.
- 74 Shen, P.-C., Su, C., Lin, Y. et al. (2021). *Nature* 593 (7858): 211–217.
- 75 Bampoulis, P., van Bremen, R., Yao, Q. et al. (2017). *ACS Appl. Mater. Interfaces* 9 (22): 19278–19286.
- 76 Sotthewes, K., van Bremen, R., Dollekamp, E. et al. (2019). *J. Phys. Chem. C* 123 (9): 5411–5420.
- 77 Liu, Y., Guo, J., Zhu, E. et al. (2018). *Nature* 557 (7707): 696–700.
- 78 Liu, X., Zhou, X., Pan, Y. et al. (2020). *Adv. Mater.* 32 (49): 2004813.

- 79 Kim, G.-S., Kim, S.-H., Park, J. et al. (2018). *ACS Nano* 12 (6): 6292–6300.
- 80 Wang, J., Yao, Q., Huang, C.-W. et al. (2016). *Adv. Mater.* 28 (37): 8302–8308.
- 81 Szabó, Á., Jain, A., Parzefall, M. et al. (2019). *Nano Lett.* 19 (6): 3641–3647.
- 82 Yang, Z., Kim, C., Lee, K.Y. et al. (2019). *Adv. Mater.* 31 (25): 1808231.
- 83 Jain, A., Szabó, Á., Parzefall, M. et al. (2019). *Nano Lett.* 19 (10): 6914–6923.
- 84 Choi, H., Moon, B.H., Kim, J.H. et al. (2019). *ACS Nano* 13 (11): 13169–13175.
- 85 Voiry, D., Mohite, A., and Chhowalla, M. (2015). *Chem. Soc. Rev.* 44 (9): 2702–2712.
- 86 Kappera, R., Voiry, D., Yalcin, S.E. et al. (2014). *Nat. Mater.* 13 (12): 1128–1134.
- 87 Cho, S., Kim, S., Kim, J.H. et al. (2015). *Science* 349 (6248): 625–628.
- 88 Mak, K.F., Lee, C., Hone, J. et al. (2010). *Phys. Rev. Lett.* 105 (13): 136805.
- 89 Lopez-Sanchez, O., Lembke, D., Kayci, M. et al. (2013). *Nat. Nanotechnol.* 8 (7): 497–501.
- 90 Geim, A.K. and Grigorieva, I.V. (2013). *Nature* 499 (7459): 419–425.
- 91 Novoselov, K.S., Mishchenko, A., Carvalho, A., and Castro Neto, A.H. (2016). *Science* 353 (6298): aac9439.
- 92 Hong, X., Kim, J., Shi, S.-F. et al. (2014). *Nat. Nanotechnol.* 9 (9): 682–686.
- 93 Akinwande, D., Petrone, N., and Hone, J. (2014). *Nat. Commun.* 5 (1): 5678.
- 94 Wang, L., Huang, L., Tan, W.C. et al. (2018). *Small Methods* 2 (3): 1700294.
- 95 Buscema, M., Groenendijk, D.J., Steele, G.A. et al. (2014). *Nat. Commun.* 5 (1): 4651.
- 96 Furchi, M.M., Pospischil, A., Libisch, F. et al. (2014). *Nano Lett.* 14 (8): 4785–4791.
- 97 Zimmermann, J.E., Axt, M., Mooshammer, F. et al. (2021). *ACS Nano* 15 (9): 14725–14731.
- 98 Bartolomeo, A.D., Genovese, L., Foller, T. et al. (2017). *Nanotechnology* 28 (21): 214002.
- 99 Furchi, M.M., Polyushkin, D.K., Pospischil, A., and Mueller, T. (2014). *Nano Lett.* 14 (11): 6165–6170.
- 100 Zhang, K., Peng, M., Yu, A. et al. (2019). *Mater. Horiz.* 6 (4): 826–833.
- 101 Huang, H., Wang, J., Hu, W. et al. (2016). *Nanotechnology* 27 (44): 445201.
- 102 Fang, H. and Hu, W. (2017). *Adv. Sci.* 4 (12): 1700323.
- 103 Yamamoto, M., Ueno, K., and Tsukagoshi, K. (2018). *Appl. Phys. Lett.* 112 (18): 181902.
- 104 Cai, Z., Cao, M., Jin, Z. et al. (2018). *NPJ 2D Mater. Appl.* 2 (1): 1–7.
- 105 Lu, X., Sun, L., Jiang, P., and Bao, X. (2019). *Adv. Mater.* 31 (50): 1902044.
- 106 Groenendijk, D.J., Buscema, M., Steele, G.A. et al. (2014). *Nano Lett.* 14 (10): 5846–5852.
- 107 Guo, W., Dong, Z., Xu, Y. et al. (2020). *Adv. Sci.* 7 (5): 1902699.
- 108 Buscema, M., Barkelid, M., Zwiller, V. et al. (2013). *Nano Lett.* 13 (2): 358–363.
- 109 Zhang, Y., Li, H., Wang, L. et al. (2015). *Sci. Rep.* 5 (1): 7938.
- 110 Freitag, M., Low, T., Xia, F., and Avouris, P. (2013). *Nat. Photonics* 7 (1): 53–59.
- 111 Mahjoub, A.M., Suzuki, S., Ouchi, T. et al. (2015). *Appl. Phys. Lett.* 107 (8): 083506.
- 112 Yan, J., Kim, M.-H., Elle, J.A. et al. (2012). *Nat. Nanotechnol.* 7 (7): 472–478.
- 113 Wu, J.-Y., Chun, Y.T., Li, S. et al. (2018). *Adv. Mater.* 30 (7): 1705880.
- 114 Xiang, D., Liu, T., Wang, J. et al. (2019). *Adv. Opt. Mater.* 7 (23): 1901115.
- 115 Zhou, C., Raju, S., Li, B. et al. (2018). *Adv. Funct. Mater.* 28 (45): 1802954.
- 116 Wu, W., Zhang, Q., Zhou, X. et al. (2018). *Nano Energy* 51: 45–53.
- 117 Gao, J., Yang, H., Mao, H. et al. (2020). *Adv. Opt. Mater.* 8 (9): 1901971.
- 118 Maiti, R., Patil, C., Saadi, M.A.S.R. et al. (2020). *Nat. Photonics* 14 (9): 578–584.
- 119 Kim, S., Maassen, J., Lee, J. et al. (2018). *Adv. Mater.* 30 (12): 1705542.
- 120 Liao, F., Deng, J., Chen, X. et al. (2020). *Small* 16 (1): 1904369.

- 121 Liang, Q., Wang, Q., Zhang, Q. et al. (2019). *Adv. Mater.* 31 (24): 1807609.
- 122 Tu, L., Cao, R., Wang, X. et al. (2020). *Nat. Commun.* 11 (1): 101.
- 123 Huo, N. and Konstantatos, G. (2017). *Nat. Commun.* 8 (1): 572.
- 124 Shin, G.H., Park, C., Lee, K.J. et al. (2020). *Nano Lett.* 20 (8): 5741–5748.
- 125 Huang, Y., Zhuge, F., Hou, J. et al. (2018). *ACS Nano* 12 (4): 4062–4073.
- 126 Lai, J., Liu, X., Ma, J. et al. (2018). *Adv. Mater.* 30 (22): 1707152.
- 127 Li, G., Yin, S., Tan, C. et al. (2021). *Adv. Funct. Mater.* 31 (40): 2104787.
- 128 Xu, H., Hao, L., Liu, H. et al. (2020). *ACS Appl. Mater. Interfaces* 12 (31): 35250–35258.
- 129 Choi, Y.-H., Kwon, G.-H., Jeong, J.-H. et al. (2019). *Appl. Surf. Sci.* 494: 37–45.
- 130 Li, C., Zhu, J., Du, W. et al. (2021). *Nanoscale Res. Lett.* 16 (1): 123.
- 131 Zhang, W., Chuu, C.-P., Huang, J.-K. et al. (2014). *Sci. Rep.* 4 (1): 3826.
- 132 Octon, T.J., Nagareddy, V.K., Russo, S. et al. (2016). *Adv. Opt. Mater.* 4 (11): 1750–1754.
- 133 Gao, W., Zhang, S., Zhang, F. et al. (2021). *Adv. Electron. Mater.* 7 (7): 2000964.
- 134 Liu, X., Li, F., Xu, M. et al. (2018). *Langmuir* 34 (47): 14151–14157.
- 135 Hussain, M., Jaffery, S.H.A., Ali, A. et al. (2021). *Sci. Rep.* 11 (1): 3688.
- 136 Viti, L., Hu, J., Coquillat, D. et al. (2015). *Adv. Mater.* 27 (37): 5567–5572.
- 137 Bolotin, K.I., Sikes, K.J., Jiang, Z. et al. (2008). *Solid State Commun.* 146 (9): 351–355.
- 138 Dean, C.R., Young, A.F., Meric, I. et al. (2010). *Nat. Nanotechnol.* 5 (10): 722–726.
- 139 Urich, A., Unterrainer, K., and Mueller, T. (2011). *Nano Lett.* 11 (7): 2804–2808.
- 140 Xia, F., Mueller, T., Lin, Y. et al. (2009). *Nat. Nanotechnol.* 4 (12): 839–843.
- 141 Cui, X., Lee, G.-H., Kim, Y.D. et al. (2015). *Nat. Nanotechnol.* 10 (6): 534–540.
- 142 Taffelli, A., Dirè, S., Quaranta, A., and Pancheri, L. (2021). *Sensors* 21 (8): 2758.
- 143 De Fazio, D., Goykhman, I., Yoon, D. et al. (2016). *ACS Nano* 10 (9): 8252–8262.
- 144 Rogalski, A. (2022). *Nat. Nanotechnol.* 17 (3): 217–219.
- 145 Konstantatos, G. (2018). *Nat. Commun.* 9 (1): 5266.
- 146 Illarionov, Y.Y., Knobloch, T., Jech, M. et al. (2020). *Nat. Commun.* 11 (1): 3385.
- 147 Akinwande, D., Huyghebaert, C., Wang, C.-H. et al. (2019). *Nature* 573 (7775): 507–518.